Research Square

Preprints are preliminary reports that have not undergone peer review.
They should not be considered conclusive, used to inform clinical practice,
or referenced by the media as validated information.

In Situ Imaging of Adjacent Biomolecules via Proximity Anchored Modules Assembly

Yuting Zou
First Affiliated Hospital of Chongqing Medical University
Zhangling Liu
First Affiliated Hospital of Chongqing Medical University
YunPeng Shu
First Affiliated Hospital of Chongqing Medical University
Shasha Zhu
First Affiliated Hospital of Chongqing Medical University
Haiping Wu
First Affiliated Hospital of Chongqing Medical University
Tiantian Yang
First Affiliated Hospital of Chongqing Medical University
Xiaoxue Cheng
Second Affiliated Hospital of Zhejiang University
Yuanyuan Huang
First Affiliated Hospital of Chongqing Medical University
Yangli Zhang
First Affiliated Hospital of Chongqing Medical University
Wenlong Ren
First Affiliated Hospital of Chongqing Medical University
Yi Zhang
First Affiliated Hospital of Chongqing Medical University
Shijia Ding
Chongqing Medical University
Wei Cheng
chengwei@hospital.cqmu.edu.cn

First Affiliated Hospital of Chongqing Medical University
Jia Li
First Affiliated Hospital of Chongqing Medical University

Method Article

Keywords: in situ imaging, multiplexed detection, proximal biomolecules, modular DNA assembly, proximity extension assay

Posted Date: April 2nd, 2026

DOI: https://doi.org/10.21203/rs.3.rs-9062242/v1

License: This work is licensed under a Creative Commons Attribution 4.0 International License. Read Full License

Additional Declarations: No competing interests reported.

Version of Record: A version of this preprint was published at Journal of Nanobiotechnology on July 5th, 2026. See the published version at https://doi.org/10.1186/s12951-026-04782-8.

Abstract

Aberrant proximal biomolecular complexes are critical disease biomarkers. The precise in situ imaging of these complexes is essential for deciphering disease pathogenesis and precision diagnostics. However, current in situ analysis technologies are often constrained by limited resolution, diffusion-mediated false positives, or the requirements for rigid conjugation between recognition and amplification moieties, which hampers versatility and multiplexing. Here, we introduce Proximity Anchored Modules Assembly (PAMA), a versatile and multiplexed imaging strategy with a “plug-and-play” architecture. By decoupling target recognition from signal amplification via programmable DNA tracks synthesized by Primer Exchange Reaction (PER), PAMA triggers a polymerase-driven extension exclusively upon dual-recognition events. This mechanism ensures precise proximity-dependent activation, showing specific signal response to homologous and heterologous targets. We further validated PAMA as a versatile platform for detection of proximal biomarkers by visualizing HER2 receptor dimerization patterns in breast cancer cells and precise discrimination of BCR-ABL^{P210} fusion gene isoforms in clinical chronic myeloid leukemia (CML) samples. PAMA bridges molecular precision with spatial context through a rapid (approximately 2.5 h) and highly sensitive in situ profiling workflow. Ultimately, PAMA establishes a versatile, modular framework for the precise imaging of diagnostic biomolecular complexes, promising to accelerate both biological discovery and precision clinical diagnostics.

Introduction

Proximal biomolecules serve as fundamental functional units that govern cellular signaling and regulatory processes.[1, 2] The dysregulation of these complexes, such as pathogenic gene fusions[3, 4] and dysregulated protein complexes,[5, 6] is a critical mechanism in various diseases, making the aberrant complexes an important class of diagnostic biomarkers. For instance, the constitutive dimerization of receptor tyrosine kinases (RTKs) is not only a hallmark of malignancy but also a key therapeutic target.[7, 8] Therefore, the ability to directly detect these proximal biomarker complexes within their native in situ environment is essential for understanding disease mechanisms and developing precision diagnostics.[9–12]

Current in situ diagnostic approaches present inherent limitations. Immunohistochemistry (IHC)[13] and fluorescence in situ hybridization (FISH)[14, 15] represent clinical standards but suffer from distinct drawbacks. IHC is labor-intensive and restricted to single biomolecular detection. While FISH is the gold standard for nucleic acids imaging, it relies on targeting extensive genomic regions. This requirement inherently compromises the sensitivity for discriminating clinically relevant fusion variants or small insertions/deletions. Although Förster resonance energy transfer (FRET)[16] offers nanometer-scale resolution, its multiplexing capability is severely constrained by spectral crosstalk and limited compatible donor-acceptor pairs. Emerging enzyme-based proximity labeling (PL) methods, such as BioID and APEX, have expanded the toolkit for profiling proximal pathogenic complexes.[17, 18] However, their

reliance on the uncontrolled diffusion of reactive intermediates fundamentally lacks the stringency required for precise biomarker diagnostic. This diffusion inevitably generates high background noise by labeling bystander molecules, obscuring the definitive identification of specific pathogenic complexes. Furthermore, the requirement for toxic co-factors (e.g., H_2O_2) or prolonged labeling times severely compromises the physiological integrity of clinical specimens.

To bridge the gap between recognition specificity and signal amplifiability, technologies such as Proximity Ligation Assays (PLA)[19] and Proximity Extension Assays (PEA)[20] have been developed. These methods utilize dual-recognition events to generate amplifiable DNA signals, significantly improving specificity. However, they typically rely on rigid designs where recognition moieties (e.g., antibodies) are covalently coupled to amplification triggers. This bioconjugation process is often labor-intensive, chemically complex, and prone to batch-to-batch heterogeneity, which can compromise the affinity and stability of the recognition domains. Moreover, this lack of modularity necessitates the complete re-synthesis and re-optimization of the entire probe set for every new target pair, severely restricting flexibility, versatility and the potential for high-order multiplexing in heterogeneous clinical samples.

Here we introduce Proximity Anchored Modules Assembly (PAMA), a modular and multiplexed in situ imaging strategy engineered specifically for the precise identification of proximal biomarkers. Unlike rigid conjugates, PAMA features a “plug-and-play” architecture comprising three interchangeable components: a specific recognition domain, a programmable DNA track synthesized via Primer Exchange Reaction (PER),[21] and a signal generation unit. As illustrated in **Scheme 1**, upon the proximal binding of two targeting modules, polymerase-driven extension initiates exclusively at interaction sites, displacing and releasing the extension strand from the shielding strand, thereby exposing docking sites for fluorescence-labeled complementary sequences. Crucially, this design ensures signal generation only upon precise dual recognition, guaranteeing high localization specificity and excellent signal-to-noise ratios. We validated PAMA as a unified platform by visualizing HER2 protein dimers in breast cancer cells and identifying BCR-ABL^{P210} fusion isoforms in clinical leukemia samples, which are critical biomarkers for precise diagnosis and guiding targeted therapeutic strategies. Using a rapid (approximately 2.5 hours) workflow, we achieved highly sensitive in situ profiling with preserved spatial context. PAMA thus establishes a versatile and modular framework for the precise imaging of diverse classes of adjacent biomolecules in complex diseases.

Scheme 1. Schematic illustration of the Proximity Anchored Modules Assembly (PAMA).

Materials and methods

Materials and instrumentation

All DNA oligonucleotides (Table S1, Supporting Information) were synthesized by Sangon Biotech. Co., Ltd. (Shanghai, China). Reagents including dATPs, dCTPs, dTTPs, dNTP Mix, RNase-free ddH_2O, RNase

Inhibitor, DEPC-treated 20× SSC buffer, formamide, and Triton X-100 were purchased from Sangon Biotech. Co. Ltd. (Shanghai, China). 1× PBS and DEPC-treated PBS were obtained from Biosharp (Hefei, China). Dulbecco's PBS and Red Blood Cell Lysis Buffer from Solarbio (Beijing, China). Enzymatic reagents, including Bst DNA Polymerase (Large Fragment), ThermoPol Reaction Buffer, NEBuffer™ 2, and Magnesium Sulfate ($MgSO_4$) solution, were sourced from New England Biolabs Inc. (Beijing, China). For cell culture, Dulbecco's Modified Eagle's Medium (DMEM), RPMI 1640 Medium, and penicillin-streptomycin were purchased from Gibco (Shanghai, China); Fetal Bovine Serum (FBS) was from ExCell (Australia). Ligands hNRG-1 and EGF were purchased from Cell Signaling Technology (Shanghai, China) and Peprotech (Rocky Hill, NJ, USA), respectively. Kits for RNA extraction and RT-PCR included the SPARKeasy Cell RNA Kit (Sparkjade, China) and PrimeScript™ One Step RT-PCR Kit Ver.2 (TaKaRa Bio, Inc., Dalian, China). All chemicals were of molecular biology grade. Fluorescence measurements for homogeneous assays were conducted using a Synergy H1 MD automatic microplate reader (Biotek, USA). Gel electrophoresis was analyzed using a Bio-Rad system (USA) and imaged with Uvidoc HD6 Touch Plus (UVITEC, UK). RNA concentration was quantified via a NanoDrop spectrophotometer (Thermo Fisher Scientific, USA). In situ fluorescence imaging was performed on a Leica DMI8 Inverted Fluorescence Microscope (Leica, Germany).

Homogeneous assay for mechanism validation and kinetics analysis: To assemble the functional module, 10 nM of Probe, S strand, and ES strand were hybridized in 1× TME buffer (10 mM Tris-HCl, pH 8.0, 12.5 mM $MgCl_2$, 1 mM EDTA) by heating at 95°C for 5 min and incubating at 37°C for 1 h. Subsequently, the target ($Target_{hom}$/$Target_{het,}$ 1 μM) was added to the module solution and incubated at 37°C for 30 min. For strand extension, a reaction mixture containing Bst DNA polymerase (4 U), dNTPs (100 μM), 1× NEBuffer™ 2, and FAM-CS (500 nM, excluded for PAGE analysis) was added. The reaction was incubated at 37°C for 30 min, followed by fluorescence measurement. Fluorescence intensity of FAM (Ex: 490 nm, Em: 520 nm) or emission spectra (500–600 nm) were recorded.

Native polyacrylamide gel electrophoresis (PAGE)

The assembly of DNA structures was characterized by 12% native PAGE. Reaction mixtures (10 μL, ~ 100 nM DNA) were mixed with loading buffer and electrophoresed in 1× TBE buffer at 110 V for 50 min. Gels were stained with GelRed for 20 min at room temperature and imaged. Detailed reactant compositions for each lane are listed in the respective figure captions.

Cell culture and ligand stimulation models

Leukemia cell lines (KCL22 and K562) were cultured in RPMI 1640 medium, while breast cancer cell lines (SK-BR-3, MCF-7, MDA-MB-231) were cultured in DMEM. Both media were supplemented with 10% FBS and 1% penicillin-streptomycin. Cells were maintained at 37°C in a humidified 5% CO_2 atmosphere. For ligand stimulation, SK-BR-3 cells were starved overnight in serum-free medium. After washing three times with ice-cold PBS, cells were treated with varying concentrations of hNRG-1 or EGF for 20 min at 37°C to induce heterodimerization. Cells were immediately washed three times with ice-cold PBS to remove excess ligands and fixed for downstream analysis.

Membrane protein-dimers in situ visualization of breast cancer cells: Cells cultured in 24-well plates were washed with ice-cold PBS and fixed with methanol/acetic acid (3:1) for 20 min at room temperature. To synthesize long DNA tracks, PER was conducted in a tube containing primers (P_{Her2}, P_{Her3}, $P_{EGFR,}$ 200 nM each), hairpins (50 nM), dHTPs (dATP, dCTP, dTTP, 100 μM each), Bst DNA polymerase (0.8 U μL^{-1}), $MgSO_4$ (10 mM), and 1× ThermoPol buffer. The reaction proceeded at 37°C for 30 min, followed by heat inactivation at 80°C for 20 min. The PER products were mixed with aptamers (Apt 2, Apt 3, Apt E; 200 nM each) in PBS and incubated with fixed cells at 37°C for 1 h. After washing three times with washing buffer (10% formamide in 2× SSC) at 37°C for 5 min, S-ES duplexes (pre-hybridized in 1× TME) were added and incubated at 37°C for 1 h. Finally, cells were incubated with an extension mixture containing Bst DNA polymerase (4 U), dNTPs (100 μM), 1× NEBuffer™ 2, and fluorescent reporters (FAM-CS/Cy3-CS/Cy5-CS, 500 nM each) at 37°C for 30 min. Nuclei were stained with DAPI prior to imaging.

Flow cytometric analysis

Fixed cells (1×10^6) were incubated with a mixture of aptamers and PER products (500 nM) in D-PBS (200 μL) at 37°C for 1 h. Unbound probes were removed by centrifugation (1000 rpm, 3 min) and washing. Cells were resuspended in binding buffer containing 1 μM S-ES duplexes and incubated at 37°C for 1 h. Following PBS washing, cells were incubated with the extension mixture (8 U Bst DNA polymerase, 100 μM dNTPs, 1×NEBuffer™ 2, and 1 μM fluorescent reporters) at 37°C for 30 min. Cells were washed, resuspended in PBS (500 μL), and 10,000 events were analyzed on a Navios Series Flow Cytometer (Beckman Coulter, China) using FlowJo software (V 10.8.1).

Isoform-specific in situ genotyping of leukemia cells: KCL22 and K562 cells (2×10^6) were fixed on slides (methanol/acetic acid, 3:1) for 20 min, washed with DEPC-treated PBS, and permeabilized with Triton X-100 (0.5% in PBS) at 37°C for 5 min. Cells were washed with PBS at 37°C for 15 min. A mixture containing PER products of primers P_{a2}, P_{e13}, and P_{e14} (1 μM) was added to the cells, heated at 95°C for 5 min (for target unmasking), and incubated at 37°C for 1 h. RNase Inhibitor (1 U μL^{-1}) was included in all reaction steps. Subsequent washing, anchoring of S-ES duplexes, and extension steps followed the PAMA protocol described above, using washing buffer (10% formamide, 2× SSC). Nuclei were stained with DAPI prior to imaging.

Clinical specimen processing and diagnostic workflow: Blood and bone marrow samples were collected from CML patients at The First Affiliated Hospital of Chongqing Medical University (Ethics approval: 2024-102-01). Samples were treated with Red Blood Cell Lysis Buffer to isolate leukocytes. The resulting cell suspension was processed following the protocol described in "*Isoform-Specific in Situ Genotyping of Leukemia Cells*."

Sanger sequencing: Total RNA was extracted using the SPARKeasy Cell RNA Kit, and concentration was determined via NanoDrop. cDNA synthesis and amplification were performed using the PrimeScript™ One Step RT-PCR Kit Ver.2. The reaction mixture (50 μL) consisted of RNA template (4 μL), each of

Forward Primers (KCL22 and K562, 1 μL) and Reverse Primer (20 μM), 2× 1-Step Buffer (25 μL), Enzyme Mix (2 μL), and RNase-free H_2O. Thermal cycling conditions were: 50°C for 30 min, 94°C for 2 min, followed by 40 cycles of [94°C/30 s, 55°C/30 s, 72°C/1 min]. PCR amplicons were submitted for Sanger sequencing.

Statistical analysis and fluorescence intensity analysis

Data are presented as mean ± standard deviation (s.d.) from at least three independent experiments (n = 3). Mean fluorescence intensity (MFI) was analyzed using ImageJ software (NIH, USA). Statistical analyses were performed using GraphPad Prism 10.1 (GraphPad Software, San Diego, CA, USA) and IBM SPSS Statistics 24.0 (IBM Corp., Armonk, NY, USA). Differences between two groups were analyzed using an unpaired two-tailed Student's t-test, whereas comparisons involving three or more groups were evaluated using a one-way analysis of variance (ANOVA). Statistical significance is indicated as ****, $P < 0.0001$, and "ns" denotes not significant.

Results and discussion

Construction and validation of PAMA in homogeneous assay

To validate the PAMA mechanism prior to its in situ application for imaging proximal biomolecules, we first constructed a simplified homogeneous assay. Since unbound probes cannot be removed in solution, we employed a "signal-off" quenching mode system. As illustrated in Fig. 1A, we designed tandem repeat models to simulate homologous ($Target_{hom}$, two identical units) and heterologous ($Target_{het}$, two distinct units) proximal targets. Upon the concurrent binding of two modules to the target, the 3' terminus of the extending strands (ES) was brought into proximity. For $Target_{hom}$ detection, a palindromic sequence was engineered at the ES 3'-terminus to facilitate self-priming and prevent false negatives. The proximity-induced ES hybridization triggered Bst DNA polymerase-mediated bi-directional extension, which displaced the original ES and exposed the S strand. This allowed a Black Hole Quencher-1 labeled complementary sequence (B-CS) to hybridize with the FAM-labeled S strand, resulting in fluorescence quenching. The 12% native PAGE analysis (Fig. 1B and 1C) was performed to monitor the stepwise assembly and extension process. Upon target binding, distinct up-shifted bands in lane 9 indicated the successful assembly of the high-molecular-weight DNA scaffolds in the presence of targets. Crucially, following the addition of Bst polymerase (lane 10), a prominent new band appeared at a lower molecular weight, which corresponds exactly to the size of the displaced, extended ES product, thereby confirming the proximity-triggered strand displacement mechanism.

Having established the structural feasibility of PAMA using these representative mimic targets, we further monitored the fluorescence signal change after adding Bst polymerase to monitor the reaction process. A significant signal reduction was observed only in the presence of all reaction components, whereas the omission of either target or polymerase abolished the response (Fig. 1D and 1F), confirming

the feasibility and specificity of the proximity-dependent extension. To achieve optimal signal-to-noise ratios, we fine-tuned the complementary overlap length at the ES 3'-terminus. Testing across five length variants demonstrated that a 6-nt overlap performed best for both target types (Fig. 1E and 1G). While longer complementary sequences stabilize base-pairing to prime extension, excessive length induces non-specific binding and background signals. Furthermore, polymerization conditions were similarly optimized (**Figure S1** and **S2**), identifying 37°C as the standard temperature, coupled with a 10-min or 30-min incubation for homologous and heterologous targets, respectively. Under these optimal conditions, we evaluated the analytical sensitivity of the system. The fluorescence intensity exhibited a concentration-dependent decrease as target concentrations increased from 0 to 50 nM (Fig. 1H). A robust linear correlation was established (Fig. 1I), with a calculated limit of detection (LOD) of 0.433 nM (3σ / slope). These results collectively demonstrate that the PAMA strategy enables sensitive and specific detection of proximal targets via polymerase-driven strand extension, establishing a solid foundation for subsequent in situ imaging.

PAMA-enabled in situ imaging of proximal HER2 dimerization

Following the validation in homogeneous solution, we adapted PAMA for the in situ visualization of spatially proximal biomolecules on cell membranes. We selected the human epidermal growth factor receptor 2 (HER2) as the model target. HER2 is frequently overexpressed in breast cancer and serves as a critical biomarker for molecular subtyping and targeted therapy of the disease.[22, 23] However, the efficacy of HER2-targeted therapies is often compromised by acquired resistance mechanisms, largely driven by the aberrant formation of homodimers or heterodimers with other ERBB family members (e.g., HER3, EGFR).[24–26] Therefore, accurately profiling the spatial organization and dimerization patterns of HER2 is essential for refining diagnostic precision and optimizing therapeutic strategies.

To achieve multiplexed in situ imaging of these proximal biomarkers, we engineered a "turn-on" detection strategy (Fig. 2A). Unlike the homogeneous assay, the S strand here is unlabeled, while the complementary strand (CS) carries a fluorophore (FAM, Cy3, or Cy5). To overcome the weak unamplified signals caused by the low cellular abundance of dimeric complexes, we employed PER to synthesize long DNA concatemers for high-contrast in situ imaging. These extended tracks provide multiple anchoring sites for S and ES strands, effectively amplifying the signal at the site of each proximal event. Gel electrophoresis analysis demonstrated the successful construction of PER products and confirmed that their length could be controlled by tuning the polymerization time. Furthermore, preliminary imaging results revealed that long PER tracks produced substantial signal enhancement compared to short, non-amplified tracks (**Figure S3** and **S4**). Meanwhile the selected aptamers[27–29] were labeled with respective fluorophores to demonstrate specific binding to HER2, HER3, and EGFR on the membrane (**Figure S5**).

We first validated the assay performance using the HER2-positive breast cancer cell line SK-BR-3 (expressing high levels of HER2/HER3 and moderate levels of EGFR).[30, 31] Negligible fluorescence was

observed in the absence of any key component (aptamers, DNA tracks, or Bst polymerase), whereas the complete system generated robust membrane-associated signals (**Figure S6-S8**). The results demonstrated the feasibility of PAMA for in situ imaging. Given that the spacing distance and steric hindrance between massive membrane proteins differ significantly from the free DNA targets used in the homogeneous assay, a longer overlap (8-nt) was required to stabilize the transient proximity and effectively prime the extension on the crowded cell surface. (**Figure S9**). To confirm specificity, we employed MDA-MB-231 (expressing high levels of EGFR and low levels of HER2/HER3) and MCF-7 (expressing low levels of HER2/HER3/EGFR) cell lines as controls.[32, 33] Fluorescence intensity analysis (Fig. 2B-D) characterized diverse receptor dimerization combinations. SK-BR-3 cells exhibited intense, punctate fluorescence signals corresponding to HER2/HER2 homodimers. In contrast, to drive the formation of heterodimers, cells were pre-incubated with their cognate ligands: human neuregulin-1 (hNRG-1)[34] and epidermal growth factor (EGF).[35] Under these induced conditions, robust HER2/HER3 (Fig. 2C) and HER2/EGFR (Fig. 2D) heterodimer signals were clearly resolved. In contrast, the control cell lines showed minimal background signal, consistent with their expression profiles. Statistical analysis of the mean fluorescence intensity (MFI) confirmed a significant deviation between the positive and negative groups. Flow cytometric analysis further corroborated the microscopic observations. As shown in **Figure S10**, a substantial rightward shift in fluorescence intensity was observed exclusively in the targeted channels for SK-BR-3 cells, confirming that the PAMA-generated signals are robustly detectable at the whole-population level, consistent with their known receptor expression profiles. Finally, we demonstrated the multiplexing capability of PAMA by simultaneously imaging HER2/HER3 and HER2/EGFR heterodimers in the same sample. As shown in Fig. 2E, the orthogonal fluorescence signals (FAM, Cy3, Cy5) allowed for the simultaneous imaging of HER2/HER3 and HER2/EGFR proximal pairs, with signal intensities significantly higher than those in negative controls. The results above confirm PAMA as a robust tool for the multiplexed dissection of membrane protein dimer landscapes.

Beyond static profiling, we further evaluated the capability of PAMA to capture dynamic shifts in dimerization levels driven by biological stimuli. We treated SK-BR-3 cells with graded concentrations of hNRG-1 and EGF respectively. As illustrated in **Fig. 3**, the in situ fluorescence signal exhibited a robust, dose-dependent increase in response to ligand titration, eventually reaching a saturation plateau. Notably, a slight signal decrease was observed under high-concentration EGF stimulation. This phenomenon is likely attributed to the intrinsic structural dynamics induced by EGF, where the EGFR/HER2 heterodimer interaction is transient and significantly weaker than EGFR homodimerization.[36] Consequently, excessive ligand stimulation might drive preferential EGFR homodimer formation or endocytosis, thereby reducing the abundance of surface-accessible heterodimers available for PAMA detection. This trend confirms that PAMA allows for the precise monitoring of receptor interplay modulation in response to extracellular signaling events.

Figure 3. Monitoring of ligand-induced modulation of HER2-related heterodimer levels. (A) Representative fluorescence images and evaluation of fluorescence signal changes of HER2/HER3 heterodimers in SK-BR-3 cells following stimulation with increasing concentrations of hNRG-1 (0-400

ng/mL). (B) Representative fluorescence images and evaluation of fluorescence signal changes of HER2/EGFR heterodimers in SK-BR-3 cells following stimulation with increasing concentrations of EGF (0-400 ng/mL). The mean fluorescence intensity (MFI) exhibited a saturable, dose-dependent increase, verifying the sensitivity of PAMA to changes in dimer abundance. Scale bar: 10 μm. Data are presented as mean ± s.d. (n = 3).

PAMA-enabled discrimination of BCR-ABL fusion isoforms

To demonstrate the universal applicability of PAMA beyond protein targets, we adapted the platform to visualize the BCR-ABL^{P210} fusion transcript, a definitive molecular hallmark of chronic myeloid leukemia (CML).[37, 38] Clinically, precise discrimination between the major isoforms (e13a2 and e14a2) is crucial (Fig. 4A), as distinct breakpoint architectures correlate with specific clinical phenotypes and therapeutic prognoses.[39, 40] We designed a “breakpoint-spanning” detection strategy illustrated in Fig. 4B. A common module (Module A) targets the ABL exon, while specific modules (Module B or C) target the BCR e13 or e14 exons, respectively. Only when the fusion transcript brings these exons into direct proximity does the bi-directional extension occur, triggering the binding of FAM-labeled CS to module A, and Cy3- or Cy5-labeled CS to modules B or C.

We first validated specificity in a homogeneous assay. Consistent with the mechanism established earlier, a fluorescence signal response was strictly dependent on the presence of all reaction components (Fig. 4C and 4D). Crucially, the system exhibited excellent specificity for the fusion transcripts. As shown in Fig. 4E and 4F, the e13a2/e14a2-targeting set yielded a significant signal only with the corresponding template, while showing negligible response to other templates or a “split” control (s-e13a2/s-e14a2, containing a 20-bp spacer). The failure of the spacer-inserted template to trigger a signal confirms that PAMA detects strict molecular proximity rather than simple co-existence.

We next evaluated the system’s performance in genotyping leukemia cell lines: KCL22 (e13a2 positive) and K562 (e14a2 positive)[41, 42], with normal white blood cells (WBCs) serving as negative controls. The specific genotypes were confirmed via Sanger sequencing (**Figure S11**). The specificity of the detection system was first corroborated by component-deletion controls using individual fluorescence channels, which showed negligible fluorescence in the absence of essential reaction components (Fig. 4G). Subsequent in situ imaging revealed that KCL22 cells exhibited dual fluorescence of FAM and Cy3 (indicating e13a2), while K562 cells displayed FAM and Cy5 signals (indicating e14a2); in contrast, WBCs remained “silent” due to the absence of the fusion gene (Fig. 4H). As the key parameter in PAMA, the 3’-terminus of (ES) was also optimized. For the in situ detection of fusion transcripts, where the RNA breakpoints bring the two modules into extremely close molecular proximity without the massive steric hindrance of membrane proteins, a shorter 5-nt overlap provided sufficient binding stability while maintaining stringent specificity. (**Figure S12**).

To translate these findings into a diagnostic criterion, we performed single-cell fluorescence intensity profiling. We analyzed the MFI of 50 individual cells from each group. 2D scatter plot analysis (Fig. 4I) revealed distinct populations. Based on the observed signal distribution, a discriminatory cut-off of MFI > 2.5 was statistically established based on the maximal separation between the negative control (WBCs) and the target-positive populations, achieving 100% classification accuracy for the cancer cell lines. This diagnostic thresholding strategy paves the way for the automated and precise identification of leukemic blasts in complex clinical specimens.

Clinical validation of PAMA for CML diagnosis and genotyping

To validate the clinical utility of PAMA, we established a streamlined workflow for the analysis of patient blood or bone marrow samples. As outlined in Fig. 5A, the optimized “sample-to-answer” process, comprising specific recognition (1 h), S-ES duplexes anchoring (1 h), and strand extension (0.5 h), was completed within approximately 2.5 hours. This rapid turnaround time significantly outpaces traditional molecular diagnostic methods (e.g., clinical kits > 18h without isoforms information),[43, 44] facilitating timely clinical decision-making.

We recruited a cohort of 60 subjects, comprising 30 BCR-ABL^{P210}-positive CML patients and 30 negative controls (clinical details in **Table S2**). In situ imaging of the BCR-ABL^{P210}-positive group (Fig. 5B) and negative group (**Figure S13**) revealed distinct, isoform-specific fluorescence patterns (FAM/Cy3 or FAM/Cy5) within the cytoplasm of positive cells, confirming the successful capture of fusion transcripts in clinical specimens. To visualize population-level discrimination, a heatmap was generated to summarize the MFI across all 60 samples (Fig. 5C). The analysis revealed a distinct segregation: the positive cohort exhibited significantly elevated MFI levels compared to the negative group. This distinction was statistically corroborated by box plot analysis (Fig. 5D), confirming that the dual-color PAMA panel enables robust segregation of leukemia patients from healthy controls.

To rigorously evaluate the diagnostic accuracy of PAMA, we first benchmarked it against qRT-PCR, the clinical gold standard for transcript quantification. We began by assessing the capability of PAMA to reflect transcript abundance. Spearman correlation analysis performed on the 30 positive samples (Fig. 5E) demonstrated strong positive associations between the BCR-ABL^{P210}/ABL copy number ratios and PAMA signal intensities (FAM: r = 0.8999; Cy3: r = 0.7857; Cy5: r = 0.8439). This suggests that the in situ fluorescence signal serves as a reliable readout for intracellular transcript abundance. Building on this quantitative fidelity, we further validated the diagnostic classification performance (Fig. 5F). The results highlight that PAMA achieves 100% concordance with qRT-PCR, yielding equivalent Sensitivity (Sen) and Specificity (Spe) for the clinical diagnosis of CML.

To contextualize these advantages, we performed a multimodal head-to-head comparison using representative clinical samples (Fig. 5G). While bone marrow smears effectively reveal morphological abnormalities (e.g., granulocyte hypercellularity), they lack molecular specificity. Similarly, FISH confirms

the presence of fusion genes via co-localization but fails to distinguish between specific isoforms (e.g., e13a2 *vs.* e14a2). Conversely, Sanger sequencing provides precise genotyping but is labor-intensive and devoid of spatial context. PAMA uniquely bridges these gaps, simultaneously providing in situ localization, isoform-specific identification, and rapid profiling.

While qRT-PCR effectively validates the quantitative fidelity of PAMA regarding overall transcript abundance, it lacks the capacity to distinguish specific breakpoint architectures. Therefore, to rigorously evaluate PAMA's capability for precise isoform subtyping, we further benchmarked its genotyping performance against Sanger sequencing as the reference standard. The performance was rigorously quantified via Receiver Operating Characteristic (ROC) analysis, yielding an Area Under the Curve (AUC) of 0.938 (Fig. 5H). Concurrently, the overall genotyping accuracy was calculated to be 96.7% and the Cohen's Kappa coefficient was calculated to be 0.902, indicating an excellent level of agreement between the PAMA assay and the reference Sanger sequencing method, confirming the reliability of PAMA for clinical genotyping (Fig. 5I). Detailed analysis of the single discordant case (Sample #29) revealed a relatively high transcript abundance (~ 8.08%), suggesting the discrepancy was not due to limited sensitivity. Instead, it highlights the challenge of matrix heterogeneity in clinical specimens: this specific sample exhibited anomalous non-specific background in the Cy5 channel, which masked the true Cy3 signal. This case highlights that while automated thresholding is efficient for population-level screening, samples with abnormal background profiles may benefit from visual inspection to distinguish true proximity-induced signals from matrix-derived noise. Collectively, these findings demonstrate the high diagnostic accuracy of PAMA, establishing it as a robust tool for the precise genotyping of leukemia.

Conclusion

In summary, we developed a PAMA strategy for the multiplexed and specific in situ analysis of adjacent biomolecules, offering a potential tool for the precise differentiation of molecular subtypes. The core innovation of PAMA lies in its modular "plug-and-play" architecture, which strategically decouples target recognition from signal amplification. Upon the specific recognition of adjacent targets by their respective recognition domains, the modules are anchored to the site, triggering a subsequent polymerase-driven bi-directional extension. Distinct proximal pairs are then resolved via distinct fluorescent indicators. By leveraging this modular architecture, PAMA successfully achieves multiplexed in situ imaging of adjacent biomolecules with flexibility and robustness.

Our results demonstrate that PAMA is not merely a detection tool but a powerful platform for in situ molecular pathology. It enabled the dynamic monitoring of ligand-induced HER2 dimerization landscapes on cell membranes and achieved the precise discrimination of BCR-ABL^{P210} fusion isoforms in clinical leukemia specimens. Notably, PAMA bridges the gap between molecular precision and spatial context, serving as a rapid (approximately 2.5 h) and highly sensitive alternative to the spatially unresolved and time-consuming sequencing methodologies. Given its high modularity, this framework can be readily expanded to visualize a diverse array of biomarkers. While this study demonstrates the

efficacy of nucleic acid-based recognition, the flexible design of the PAMA framework holds the potential to accommodate other classes of affinity ligands, including antibodies or nanobodies, for a wider range of biological applications. These features position PAMA as a versatile platform for in situ analysis, accelerating discoveries in both fundamental cell biology and precision clinical diagnostics.

Declarations

Ethics approval and consent to participate

Blood and bone marrow samples were collected from CML patients at The First Affiliated Hospital of Chongqing Medical University (Ethics approval: 2024-102-01).

Consent for publication

Not applicable.

Availability of data and materials

All data generated or analysed during this study are included in this published article and its supplementary information files.

Competing interests

The authors declare no competing interests.

Funding

The authors acknowledge financial support from the projects of the National Natural Science Foundation of China (U24A20751, 82202634, 82402750, and 82372334); the Natural Science Foundation of Chongqing, China (CSTB2023NSCQ-LZX0022); Chongqing Technological Innovation and Application Development Major Projects (CSTB2025TIAD- KPX0004); The Special Funding Project of Chongqing Municipality (2023CQBSHTB3058); Chongqing Medical Young Talents Project (YXQN202435); Science and Technology Research Project of Chongqing Education Commission (KJQN202400411); China Postdoctoral Science Foundation (2024MD764067); Research grant from Jinfeng Laboratory (JFLKYXM202403AZ-101); Young Top Talent Project of the First Affiliated Hospital of Chongqing Medical University (BJRC2022-02); Chongqing medical scientific research project (Joint project of Chongqing Health Commission and Science and Technology Bureau) (2026MSXM033).

Authors' contributions

Y.Z. and Z.L. performed all experimental work. Y.S., S.Z and H.W conducted data analysis. T.Y., X.C., Y.H. and Y.Z. collected clinical samples. W.R., Y.Z. and S.D. revised the manuscript and provided project guidance. J.L. procured funding and data curation. All authors read and approved the final manuscript.

Y.Z., Z.L.and J.L. conceived and designed the study. Y.Z. performed the experiments. Y.Z., Z.L.and J.L. conducted data processing and contributed to analysis and interpretation of data. Y.S., S.Z and H.W conducted the investigation. T.Y., X.C. and Y.H., provided resources for all experiments. Y.Z., W.R., S.D. performed data curation and validation. J.L. and W.C. supervised the overall study. W.C., J.L., Z.L. and H.W. were responsible for the project administration and funding acquisition. Y.Z., J.L. and W.C. grafted and edited the manuscript. All the authors read and approved the final manuscript.

Acknowledgements

Not applicable.

Authors' information (optional)

Y. Z., Y. S., S. ., H. W., T. Y., Y. H., Y. Z., W. R., W. C., J. L.

The Center for Clinical Molecular Medical Detection, Engineering Research Center of Chongqing Education Commission of China for IVD Technology Innovation and Translation, Laboratory Medicine Center, The First Affiliated Hospital of Chongqing Medical University, Chongqing 400016, P. R. China

Z. L., Y. Z.

Biobank, The First Affiliated Hospital of Chongqing Medical University, Chongqing 400016, P. R. China

H. W.

Sichuan-Chongqing Joint Key Laboratory for Pathology and Laboratory Medicine, Jinfeng Laboratory, Chongqing 400039, P. R. China

X. C.

Department of Laboratory Medicine, The Second Affiliated Hospital of Zhejiang University, Hangzhou, 310000, P. R. China

S. D.

Key Laboratory of Clinical Laboratory Diagnostics (Ministry of Education), College of Laboratory Medicine, Chongqing Medical University, Chongqing 400016, P. R. China

References

1. Kuna RS, Kumar A, Wessendorf-Rodriguez KA, Galvez H, Green CR, McGregor GH, Cordes T, Shaw RJ, Svensson RU, Metallo CM. Inter-Organelle Cross-Talk Supports Acetyl-Coenzyme A Homeostasis and Lipogenesis under Metabolic Stress. Sci Adv. 2023;9(18). https://doi.org/10.1126/sciadv.adf0138.

2. Keenan SN, Watt MJ, Montgomery MK. Inter-Organelle Communication in the Pathogenesis of Mitochondrial Dysfunction and Insulin Resistance. Curr Diab Rep. 2020;20(6):20. https://doi.org/10.1007/s11892-020-01300-4.
3. Gkountakos A, Singhi AD, Westphalen CB, Scarpa A, Luchini C. Fusion Genes in Pancreatic Tumors. Trends Cancer. 2024;10(5):430–43. https://doi.org/10.1016/j.trecan.2024.01.009.
4. Wang J, Ma H-L, Liu W-R, Peng Y, Zhou J-K, Yang J-L. CircBA1 Derived from BCR-ABL Fusion Gene Inhibits Cell Proliferation in Chronic Myeloid Leukemia. Cancer Commun. 2021;41(1):79–82. https://doi.org/10.1002/cac2.12120.
5. Lee H-W, Choi B, Kang HN, Kim H, Min A, Cha M, Ryu JY, Park S, Sohn J, Shin K, Yun MR, Han JY, Shon MJ, Jeong C, Chung J, Lee S-H, Im S-A, Cho BC, Yoon T-Y. Profiling of Protein–Protein Interactions via Single-Molecule Techniques Predicts the Dependence of Cancers on Growth-Factor Receptors. Nat Biomed Eng. 2018;2(4):239–53. https://doi.org/10.1038/s41551-018-0212-3.
6. Till NA, Ramanathan M, Bertozzi CR. Induced Proximity at the Cell Surface. Nat Biotechnol. 2025;43(5):702–11. https://doi.org/10.1038/s41587-025-02592-1.
7. Katoh M, Loriot Y, Brandi G, Tavolari S, Wainberg ZA, Katoh MFGFR-T, Therapeutics. Clinical Activity, Mechanisms of Resistance and New Directions. Nat Rev Clin Oncol. 2024;21(4):312–29. https://doi.org/10.1038/s41571-024-00869-z.
8. Wakano M, Tsunoda M, Murayama K, Morimoto J, Ueki R, Aoyama-Ishiwatari S, Hirabayashi Y, Asanuma H, Sando S. Reversible Optical Control of Receptor Tyrosine Kinase Activity and ERK Dynamics Using Azobenzene-Carrying DNA Aptamer Agonist. J Am Chem Soc. 2025;147(13):11477–84. https://doi.org/10.1021/jacs.5c01559.
9. Shi H, Wang Y, Zheng J, Ning L, Huang Y, Sheng A, Chen T, Xiang Y, Zhu X, Li G. Dual-Responsive DNA Nanodevice for the Available Imaging of an Apoptotic Signaling Pathway in Situ. ACS Nano. 2019;13(11):12840–50. https://doi.org/10.1021/acsnano.9b05082.
10. Yu M, Shang J, Xie C, Jiang Y, Wang Y, Liu X, Wang F. An Integrated Sequential-Activated DNA Circuit for Reliable Imaging of Intracellular miRNA and Remote Control of Cellular Function. Adv Funct Mater. 2025;35(46):2508992. https://doi.org/10.1002/adfm.202508992.
11. Liu Y, Sundah NR, Ho NRY, Shen WX, Xu Y, Natalia A, Yu Z, Seet JE, Chan CW, Loh TP, Lim BY, Shao H. Bidirectional Linkage of DNA Barcodes for the Multiplexed Mapping of Higher-Order Protein Interactions in Cells. Nat Biomed Eng. 2024;8(7):909–23. https://doi.org/10.1038/s41551-024-01225-3.
12. Passaro A, Bakir MA, Hamilton EG, Diehn M, André F, Roy-Chowdhuri S, Mountzios G, Wistuba II, Swanton C, Peters S. Cancer Biomarkers: Emerging Trends and Clinical Implications for Personalized Treatment. Cell. 2024;187(7):1617–35. https://doi.org/10.1016/j.cell.2024.02.041.
13. Yatabe Y, Dacic S, Borczuk AC, Warth A, Russell PA, Lantuejoul S, Beasley MB, Thunnissen E, Pelosi G, Rekhtman N, Bubendorf L, Mino-Kenudson M, Yoshida A, Geisinger KR, Noguchi M, Chirieac LR, Bolting J, Chung J-H, Chou T-Y, Chen G, Poleri C, Lopez-Rios F, Papotti M, Sholl LM, Roden AC, Travis WD, Hirsch FR, Kerr KM, Tsao M-S, Nicholson AG, Wistuba I, Moreira AL. Best Practices

Recommendations for Diagnostic Immunohistochemistry in Lung Cancer. J Thorac Oncol. 2019;14(3):377–407. https://doi.org/10.1016/j.jtho.2018.12.005.

14. Dos Santos M, Backer S, Saintpierre B, Izac B, Andrieu M, Letourneur F, Relaix F, Sotiropoulos A, Maire P. Single-Nucleus RNA-Seq and FISH Identify Coordinated Transcriptional Activity in Mammalian Myofibers. Nat Commun. 2020;11(1):5102. https://doi.org/10.1038/s41467-020-18789-8.
15. Goh JJL, Chou N, Seow WY, Ha N, Cheng CPP, Chang Y-C, Zhao ZW, Chen KH. Highly Specific Multiplexed RNA Imaging in Tissues with Split-FISH. Nat Methods. 2020;17(7):689–93. https://doi.org/10.1038/s41592-020-0858-0.
16. Shi L, Yang C, Zhang M, Li K, Wang K, Jiao L, Liu R, Wang Y, Li M, Wang Y, Ma L, Hu S, Bian X. Dissecting the Mechanism of Atlastin-Mediated Homotypic Membrane Fusion at the Single-Molecule Level. Nat Commun. 2024;15(1). https://doi.org/10.1038/s41467-024-46919-z.
17. Qin W, Cho KF, Cavanagh PE, Ting AY. Deciphering Molecular Interactions by Proximity Labeling. Nat Methods. 2021;18(2):133–43. https://doi.org/10.1038/s41592-020-01010-5.
18. Albright S, Cacace M, Tivon Y, Deiters A. Cell Surface Labeling and Detection of Protein Tyrosine Kinase 7 via Covalent Aptamers. J Am Chem Soc. 2023;145(30):16458–63. https://doi.org/10.1021/jacs.3c02752.
19. Di Giusto DA, Wlassoff WA, Gooding JJ, Messerle BA, King GC. Proximity Extension of Circular DNA Aptamers with Real-Time Protein Detection. Nucleic Acids Res. 2005;33(6):e64. https://doi.org/10.1093/nar/gni063.
20. Lundberg M, Eriksson A, Tran B, Assarsson E, Fredriksson S. Homogeneous Antibody-Based Proximity Extension Assays Provide Sensitive and Specific Detection of Low-Abundant Proteins in Human Blood. Nucleic Acids Res. 2011;39(15):e102–102. https://doi.org/10.1093/nar/gkr424.
21. Kishi JY, Schaus TE, Gopalkrishnan N, Xuan F, Yin P. Programmable Autonomous Synthesis of Single-Stranded DNA. Nat Chem. 2018;10(2):155–64. https://doi.org/10.1038/nchem.2872.
22. Schettini F, Pascual T, Conte B, Chic N, Brasó-Maristany F, Galván P, Martínez O, Adamo B, Vidal M, Muñoz M, Fernández-Martinez A, Rognoni C, Griguolo G, Guarneri V, Conte PF, Locci M, Brase JC, Gonzalez-Farre B, Villagrasa P, De Placido S, Schiff R, Veeraraghavan J, Rimawi MF, Osborne CK, Pernas S, Perou CM, Carey LA, Prat A. HER2-Enriched Subtype and Pathological Complete Response in HER2-Positive Breast Cancer: A Systematic Review and *Meta*-Analysis. Cancer Treat Rev. 2020;84:101965. https://doi.org/10.1016/j.ctrv.2020.101965.
23. Liu C, Sun L, Niu N, Hou P, Chen G, Wang H, Zhang Z, Jiang X, Xu Q, Zhao Y, Wang Y, Shi Y, Liu M, Yang Y, Qian W, Wang J, Liu C. Molecular Classification of Hormone Receptor-Positive /HER2-Positive Breast Cancer Reveals Potential Neoadjuvant Therapeutic Strategies. Signal Transduct Target Ther. 2025;10(1):97. https://doi.org/10.1038/s41392-025-02181-3.
24. Azad A, Arshad M, Generali D, Feldinger K, Gijsen M, Strina C, Cappelletti M, Andreis D, Leek R, Haider S, Kellokumpu-Lehtinen P-L, Roxanis I, Harris AL, Shaaban AM, Joensuu H, Kong A. PTPN9 Regulates HER3 Phosphorylation during Trastuzumab Treatment and Loss of PTPN9 Is a Potential

Biomarker for Trastuzumab Resistance in HER2 Positive Breast Cancer. Cancer Commun. 2024;45(1):68–73. https://doi.org/10.1002/cac2.12632.

25. Yang L, Bhattacharya A, Peterson D, Li Y, Liu X, Marangoni E, Robila V, Zhang Y. Targeted Dual Degradation of HER2 and EGFR Obliterates Oncogenic Signaling, Overcomes Therapy Resistance, and Inhibits Metastatic Lesions in HER2-Positive Breast Cancer Models. Drug Resist Updat. 2024;74:101078. https://doi.org/10.1016/j.drup.2024.101078.
26. Kumagai S, Koyama S, Nishikawa H. Antitumour Immunity Regulated by Aberrant ERBB Family Signalling. Nat Rev Cancer. 2021;21(3):181–97. https://doi.org/10.1038/s41568-020-00322-0.
27. Sett A, Borthakur BB, Bora U. Selection of DNA Aptamers for Extra Cellular Domain of Human Epidermal Growth Factor Receptor 2 to Detect HER2 Positive Carcinomas. Clin Transl Oncol. 2017;19(8):976–88. https://doi.org/10.1007/s12094-017-1629-y.
28. Wang D-L, Song Y-L, Zhu Z, Li X-L, Zou Y, Yang H-T, Wang J-J, Yao P-S, Pan R-J, Yang CJ, Kang D-Z. Selection of DNA Aptamers against Epidermal Growth Factor Receptor with High Affinity and Specificity. Biochem Biophys Res Commun. 2014;453(4):681–5. https://doi.org/10.1016/j.bbrc.2014.09.023.
29. Xu L, Liu S, Yang T, Shen Y, Zhang Y, Huang L, Zhang L, Ding S, Song F, Cheng W. DNAzyme Catalyzed Tyramide Depositing Reaction for *In Situ* Imaging of Protein Status on the Cell Surface. Theranostics. 2019;9(7):1993–2002. https://doi.org/10.7150/thno.31943.
30. Henjes F, Bender C, von der Heyde S, Braun L, Mannsperger HA, Schmidt C, Wiemann S, Hasmann M, Aulmann S, Beissbarth T, Korf U. Strong EGFR Signaling in Cell Line Models of ERBB2-Amplified Breast Cancer Attenuates Response towards ERBB2-Targeting Drugs. Oncogenesis. 2012;1(7):e16–16. https://doi.org/10.1038/oncsis.2012.16.
31. DeFazio-Eli L, Strommen K, Dao-Pick T, Parry G, Goodman L, Winslow J. Quantitative Assays for the Measurement of HER1-HER2 Heterodimerization and Phosphorylation in Cell Lines and Breast Tumors: Applications for Diagnostics and Targeted Drug Mechanism of Action. Breast Cancer Res. 2011;13(2):R44. https://doi.org/10.1186/bcr2866.
32. Spaziani S, Esposito A, Barisciano G, Quero G, Elumalai S, Leo M, Colantuoni V, Mangini M, Pisco M, Sabatino L, De Luca AC, Cusano A. Combined SERS-Raman Screening of HER2-Overexpressing or Silenced Breast Cancer Cell Lines. J Nanobiotechnol. 2024;22(1):350. https://doi.org/10.1186/s12951-024-02600-7.
33. Smith SE, Mellor P, Ward AK, Kendall S, McDonald M, Vizeacoumar FS, Vizeacoumar FJ, Napper S, Anderson DH. Molecular Characterization of Breast Cancer Cell Lines through Multiple Omic Approaches. Breast Cancer Res. 2017;19(1):65. https://doi.org/10.1186/s13058-017-0855-0.
34. Diwanji D, Trenker R, Thaker TM, Wang F, Agard DA, Verba KA, Jura N. Structures of the HER2–HER3–NRG1β Complex Reveal a Dynamic Dimer Interface. Nature. 2021;600(7888):339–43. https://doi.org/10.1038/s41586-021-04084-z.
35. Patel D, Bassi R, Hooper A, Prewett M, Hicklin DJ, Kang X. Anti-Epidermal Growth Factor Receptor Monoclonal Antibody Cetuximab Inhibits EGFR/HER-2 Heterodimerization and Activation. Int J

Oncol. 2009;34(1):25–32. https://doi.org/10.3892/ijo_00000125.

36. Bai X, Sun P, Wang X, Long C, Liao S, Dang S, Zhuang S, Du Y, Zhang X, Li N, He K, Zhang Z. Structure and Dynamics of the EGFR/HER2 Heterodimer. Cell Discov. 2023;9:18. https://doi.org/10.1038/s41421-023-00523-5.
37. Cully M. Belt and Braces for BCR–ABL. Nat Rev Drug Discov. 2017;16(5):313–313. https://doi.org/10.1038/nrd.2017.79.
38. Shammas T, Peiris MN, Meyer AN, Donoghue DJ. BCR-ABL: The Molecular Mastermind behind Chronic Myeloid Leukemia. Cytokine Growth Factor Rev. 2025;83:45–58. https://doi.org/10.1016/j.cytogfr.2025.05.001.
39. Elbjeirami WM, Alabdulwahab AS, ELSayed HG, Abdelghaffer NA, Elnagdi N, Al-Jedani H, Abd Allatif N, Al Shaikh A, Al-Allaf F. Response to Imatinib in E13a2 Versus E14a2 BCR-ABL Fusion Transcripts in Chronic Myeloid Leukemia Saudi Patients. Blood. 2016;128(22):5453–5453. https://doi.org/10.1182/blood.V128.22.5453.5453.
40. Baccarani M, Castagnetti F, Gugliotta G, Rosti G, Soverini S, Albeer A, Pfirrmann M. The Proportion of Different BCR-ABL1 Transcript Types in Chronic Myeloid Leukemia. Int Overv Leukemia. 2019;33(5):1173–83. https://doi.org/10.1038/s41375-018-0341-4.
41. Mundhada S, Luthra R, Cano P. Association of HLA Class I and Class II Genes with Bcr-Abl Transcripts in Leukemia Patients with t(9;22) (Q34;Q11). BMC Cancer. 2004;4(1):25. https://doi.org/10.1186/1471-2407-4-25.
42. Rapozzi V, Xodo LE. Efficient Silencing of Bcr/Abl Oncogene by Single- and Double-Stranded siRNAs Targeted against B2a2 Transcripts. Biochemistry. 2004;43(51):16134–41. https://doi.org/10.1021/bi048634w.
43. Dewald GW, Wyatt WA, Juneau AL, Carlson RO, Zinsmeister AR, Jalal SM, Spurbeck JL, Silver RT. Highly Sensitive Fluorescence In Situ Hybridization Method to Detect Double BCR/ABL Fusion and Monitor Response to Therapy in Chronic Myeloid Leukemia. Blood. 1998;91(9):3357–65. https://doi.org/10.1182/blood.V91.9.3357.
44. Tkachuk DC, Westbrook CA, Andreeff M, Donlon TA, Cleary ML, Suryanarayan K, Homge M, Redner A, Gray J, Pinkel D. Detection of Bcr-Abl Fusion in Chronic Myelogeneous Leukemia by in Situ Hybridization. Science. 1990;250(4980):559–62. https://doi.org/10.1126/science.2237408.

Schemes

Scheme 1 is available in the Supplementary Files section

Figures

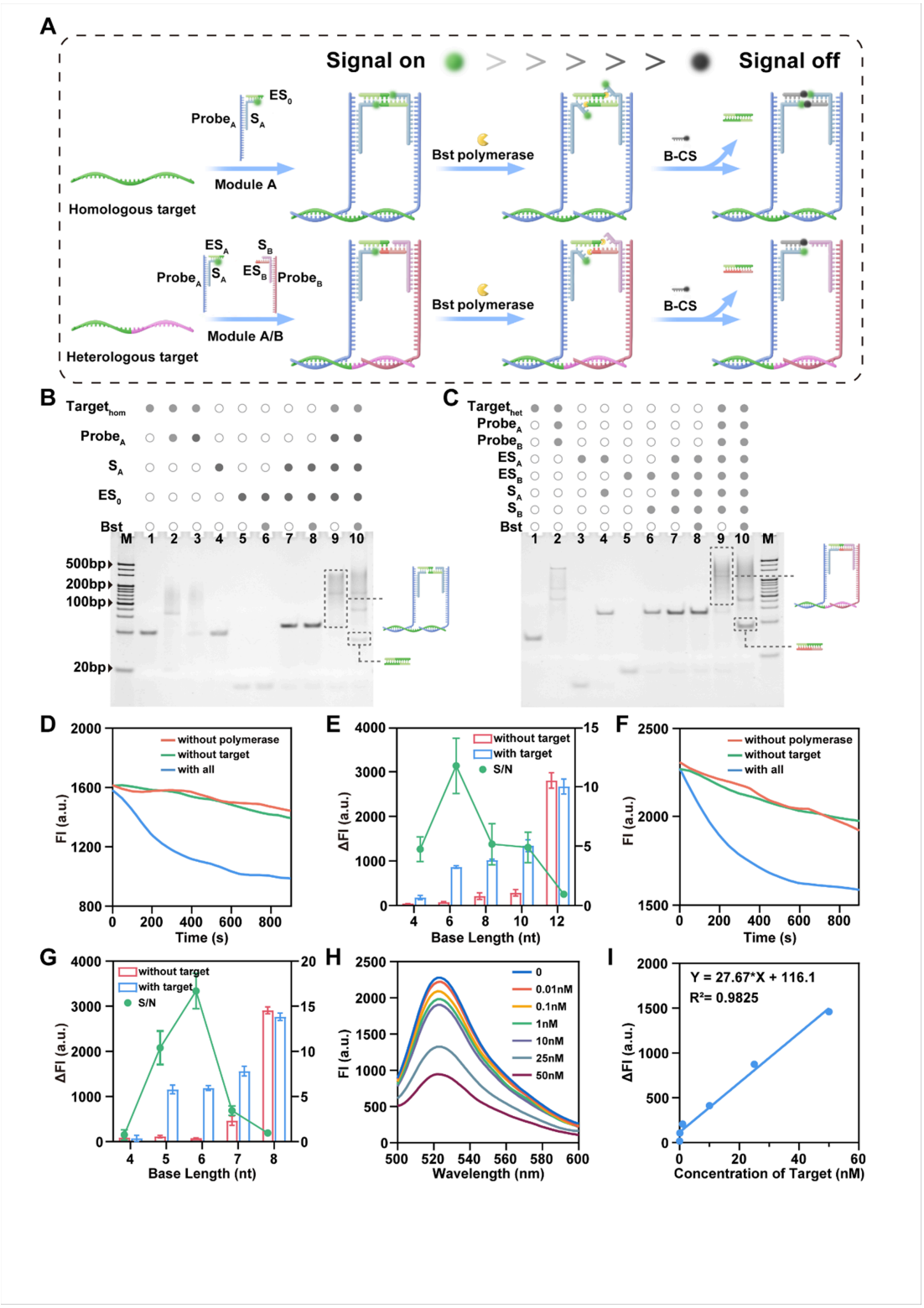


Figure 1

Validation of the PAMA strategy in a homogeneous assay. (A) Schematic illustration of the PAMA mechanism operating in a “signal-off” reporting mode. Native PAGE (12%) analysis of the assembly and extension products triggered by homologous (B) and heterologous (C) targets. The composition of each lane is indicated by the matrix above the gel; filled circles denote the presence of components. Darker circles indicate a two-fold concentration relative to lighter circles, simulating the stoichiometric binding

of two modules to a single target. For homologous targets: real-time fluorescence kinetics monitoring the quenching effect (D) and optimization of the palindromic overlap length at the 3’-terminus of the ES strand (E). For heterologous targets: real-time fluorescence kinetics (F) and optimization of the complementary overlap length at the 3’-terminus of the ES strand (G). (H) Fluorescence emission spectra in response to varying target concentrations ranging from 0 to 50 nM. (I) Linear calibration curve plotting the fluorescence intensity change (ΔFI) against target concentration ranging from 0 to 50 nM. ΔFI represents the net reduction in fluorescence intensity relative to the initial state (F_0 - F). Error bars represent the standard deviation of three independent replicates (n = 3).

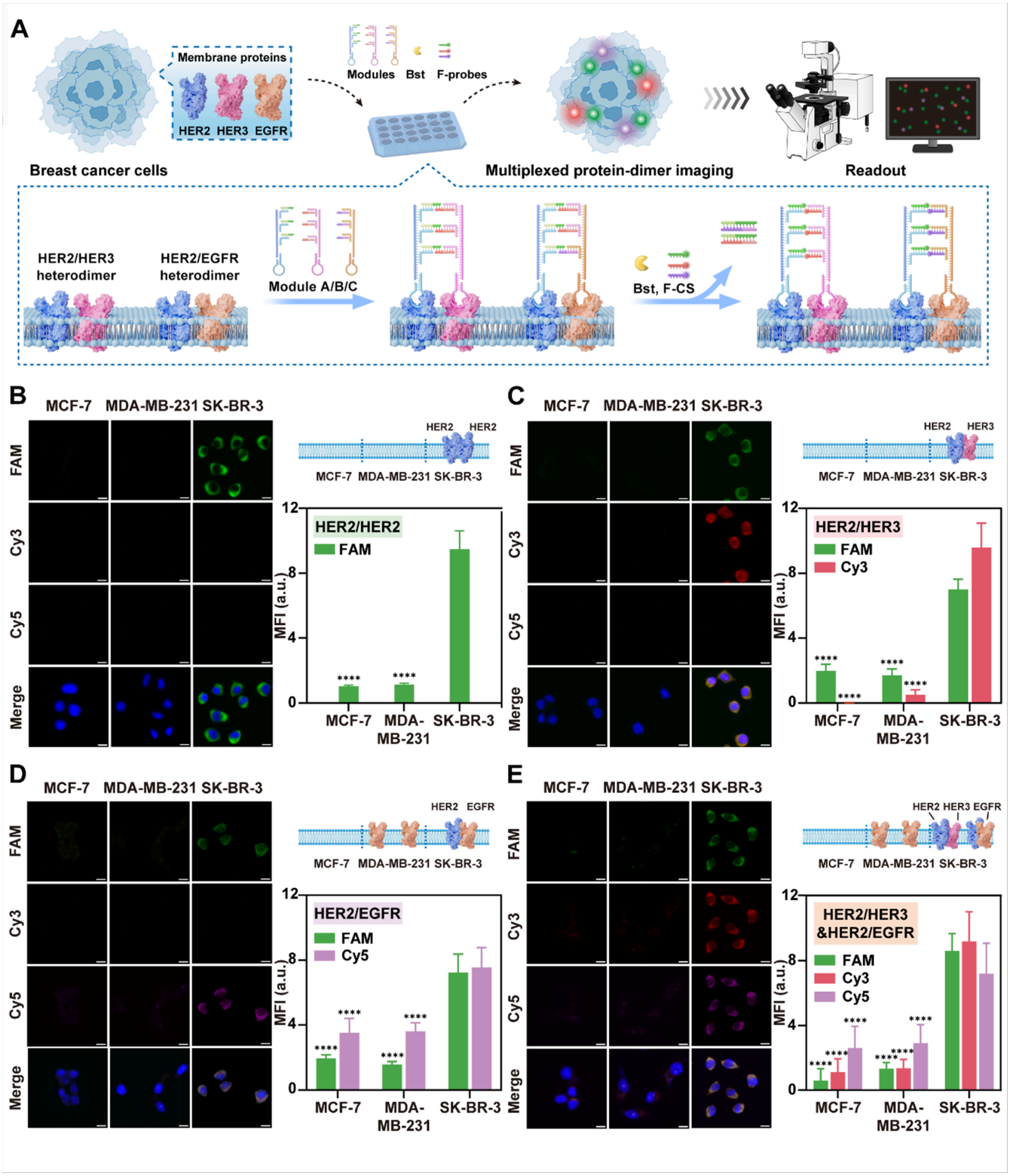


Figure 2

In situ multiplexed visualization of HER2 dimerization patterns in breast cancer cell lines. (A) Schematic illustration of the “turn-on” PAMA strategy for the specific imaging of proximal HER2 dimers on the cell membrane. Representative fluorescence images and corresponding statistical analysis of specific dimerization events: HER2 homodimers (B), HER2/HER3 heterodimers (C), and HER2/EGFR heterodimers (D). (E) Simultaneous and multiplexed imaging and statistical analysis of HER2/HER3 and

HER2/EGFR heterodimers within the same cellular context. Fluorescence channels: 405 nm (DAPI, nucleus, blue), 488 nm (FAM, green), 547 nm (Cy3, red), and 642 nm (Cy5, magenta). All images were acquired using a 40× objective; scale bar: 10 μm. Data are presented as mean ± standard deviation (s.d., n = 3 independent experiments). Statistical significance: ****, $P < 0.0001$.

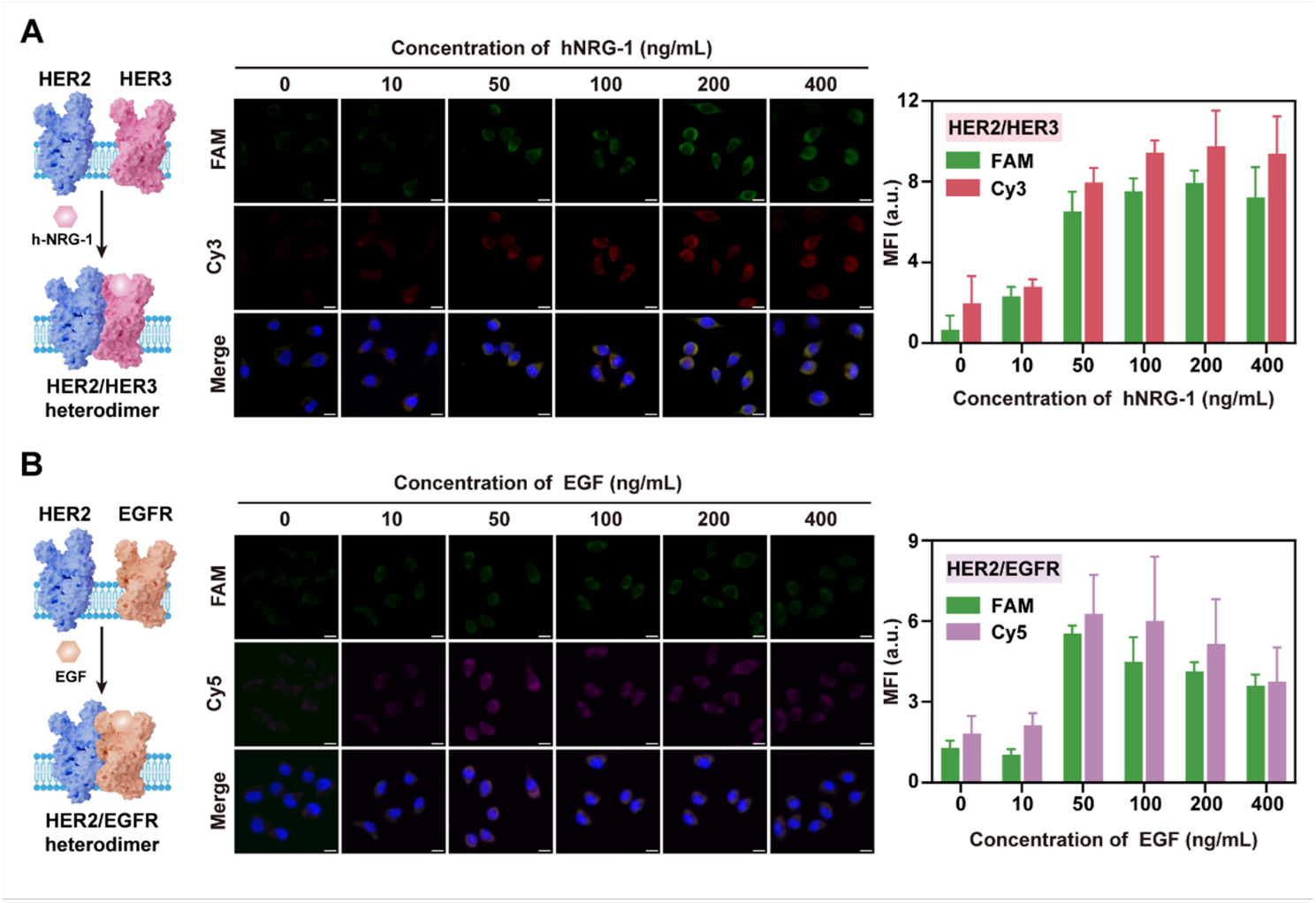


Figure 3

Monitoring of ligand-induced modulation of HER2-related heterodimer levels. (A) Representative fluorescence images and evaluation of fluorescence signal changes of HER2/HER3 heterodimers in SK-BR-3 cells following stimulation with increasing concentrations of hNRG-1 (0-400 ng/mL). (B) Representative fluorescence images and evaluation of fluorescence signal changes of HER2/EGFR heterodimers in SK-BR-3 cells following stimulation with increasing concentrations of EGF (0-400 ng/mL). The mean fluorescence intensity (MFI) exhibited a saturable, dose-dependent increase, verifying the sensitivity of PAMA to changes in dimer abundance. Scale bar: 10 μm. Data are presented as mean ± s.d. (n = 3).

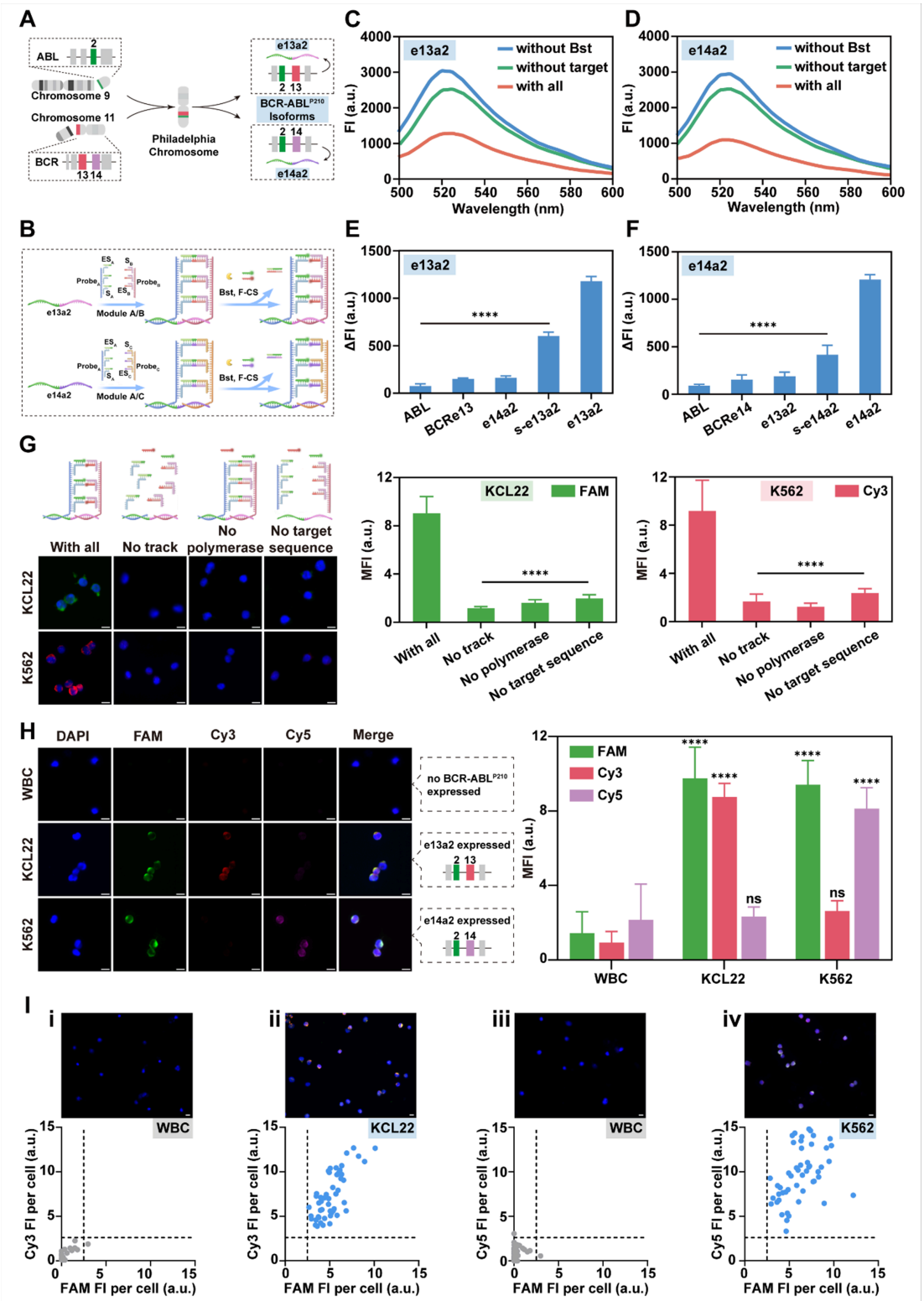


Figure 4

PAMA-based in situ genotyping of BCR-ABL^{P210} fusion isoforms. (A) Schematic representation of the chromosomal translocation forming the BCR-ABL^{P210} fusion gene and its major isoforms (e13a2 and e14a2). (B) Working principle of the isoform-specific PAMA assay. Proximity between the common ABL module and specific BCR modules at the fusion breakpoint triggered orthogonal fluorescence signals. (C, D) Feasibility validation in homogeneous assay showing signal dependence on all reaction

components for e13a2 and e14a2. (E, F) Specificity analysis demonstrating discrimination between isoforms and controls. (G) Control experiments in KCL22 and K562 cells showing negligible signal in the absence of tracks, targets, or polymerase. (H) Representative in situ multiplexed imaging and statistical evaluation of fusion isoforms in normal WBCs, KCL22, and K562 cells. (I) Establishment of diagnostic thresholds via single-cell analysis. (i–iv) 2D scatter plots mapping the fluorescence intensity of FAM *vs*. Cy3 (for WBC/KCL22) and FAM *vs*. Cy5 (for WBC/K562). The dashed lines indicate the empirical cut-off values (MFI = 2.5) used to distinguish positive leukemia cells from normal leukocytes. Scale bar: 10 μm. Data are presented as mean ± s.d. (n = 3). Statistical significance: ****, $P < 0.0001$; ns, not significant.

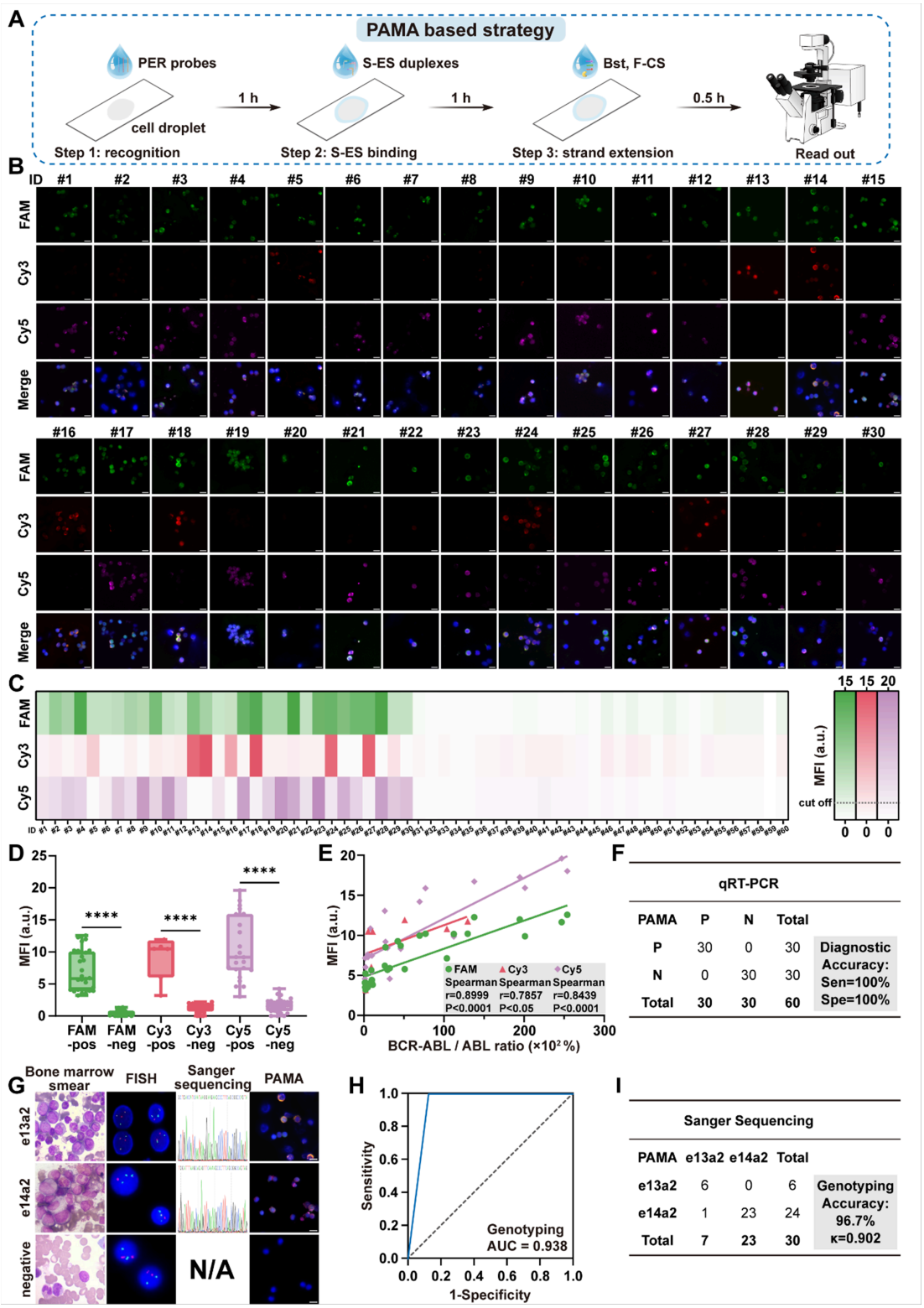


Figure 5

Clinical validation of PAMA for the diagnosis and genotyping of CML. (A) Schematic workflow of the PAMA in situ assay, illustrating the rapid 2.5-hour timeline from sample recognition to signal output. (B) Representative fluorescence microscope images of blood or bone marrow specimens from the BCR-ABL^{P210}-positive cohort (n = 30). Distinct fluorescence channels indicate the specific fusion isoforms detected in situ. (C) Heatmap visualization of the mean fluorescence intensity (MFI) profile across the

clinical cohort (n = 60; 30 positive, 30 negative). (D) Statistical comparison of MFI levels between BCR-ABL^{P210}-positive and negative groups. Data are presented as box-and-whisker plots; ****, $P < 0.0001$. (E) Spearman correlation analysis between PAMA fluorescence intensity (FAM and Cy3/Cy5 channels) and BCR-ABL^{P210}/ABL copy number ratios determined by qRT-PCR (n = 30). (F) Confusion matrix highlighting the diagnostic performance metrics of PAMA versus qRT-PCR. (G) Multimodal benchmarking of PAMA against standard diagnostic methods (Bone marrow smear, FISH, and Sanger sequencing), demonstrating PAMA's unique integration of molecular specificity and spatial context. (H) Receiver Operating Characteristic (ROC) curve analysis assessing the diagnostic accuracy of PAMA for fusion genotype classification (n = 30, AUC = 0.938). (I) Confusion matrix comparing BCR-ABL^{P210} isoform genotyping results between PAMA and Sanger sequencing.

Supplementary Files

This is a list of supplementary files associated with this preprint. Click to download.

- SupportingInformationJNB.docx
- image1.jpeg